Non-uniform lateral current distribution in quantum cascade lasers

Xue Huang,[1,2,*] **Yamac Dikmelik,**[3] **and Claire Gmachl**[1]

[1]*Department of Electrical Engineering, Princeton University, Princeton, NJ 08544, USA*
[2]*current at Department of Electrical Engineering, Yale University, New Haven, CT 06511, USA*
[3]*Department of Electrical and Computer Engineering, Johns Hopkins University, Baltimore, MD 21218, USA*
[*]*xuehuang@princeton.edu*

Abstract: Non-uniform lateral current distribution in quantum cascade (QC) lasers is investigated, as a result of stimulated-optical-emission-assisted electron transport, the rate of which depends on the local photon density and is comparable to the longitudinal optical (LO) phonon scattering rate. A microscopic model based on rate equations is built to study the self-consistent process of interaction between local electrons and photons in QC lasers. The non-uniform distribution of lateral current and the corresponding spatial hole burning are simulated from this model. Moreover, multi-transverse-mode operation in QC lasers is also investigated.

© 2014 Optical Society of America

OCIS codes: (140.5965) Semiconductor lasers, quantum cascade; (270.3430) Laser theory.

References and links

1. M. D. Escarra, A. Benz, A. M. Bhatt, A. J. Hoffman, X. Wang, J. Y. Fan, and C. Gmachl, "Thermoelectric effect in quantum cascade lasers," IEEE Photonics J. **2**, 500–509 (2010).
2. A. Lops, V. Spagnolo, and G. Scamarcio, "Thermal modeling of GaInAs/AlInAs quantum cascade lasers," J. Appl. Phys. **100**, 043109 (2006).
3. W. W. Bewley, J. R. Lindle, C. S. Kim, I. Vurgaftman, J. R. Meyer, A. J. Evans, J. S. Yu, S. Slivken, and M. Razeghi, "Beam steering in high-power CW quantum-cascade lasers," IEEE J. Quantum Electron. **41**, 833–841 (2005).
4. Q. Yang, M. Kinzer, F. Fuchs, S. Hugger, B. Hinkov, W. Bronner, R. Lösch, R. Aidam, and J. Wagner, "Beam steering and lateral hole burning in mid-infrared quantum-cascade lasers," Phys. Status Solidi C **9**, 302–305 (2012).
5. N. Yu, L. Diehl, E. Cubukcu, D. Bour, S. Corzine, G. Hföler, A. K. Wojcik, K. B. Crozier, A. Belyanin, and F. Capasso, "Coherent coupling of multiple transverse modes in quantum cascade lasers," Phys. Rev. Lett. **102**, 013901 (2009).
6. A. K. Wojcik, N. Yu, L. Diehl, F. Capasso, and A. Belyanin, "Self-synchronization of laser modes and multistability in quantum cascade lasers," Phys. Rev. Lett. **106**, 133902 (2011).
7. Z.-M. S. Li, Y.-Y. Li, and G.-P. Ru, "Simulation of quantum cascade lasers," J. Appl. Phys. **110**, 093109 (2011).
8. C. Sirtori, F. Capasso, J. Faist, A. L. Hutchinson, D. L. Sivco, and A. Y. Cho, "Resonant tunneling in quantum cascade lasers," IEEE J. Quantum Electron. **34**, 1722–1729 (1998).
9. Y. Yao, Z. Liu, A. J. Hoffman, K. J. Franz, and C. F. Gmachl, "Voltage tenability of quantum cascade lasers," IEEE J. Quantum Electron. **45**, 730–736 (2009).
10. S. Kumar and Q. Hu, "Coherence of resonant-tunneling transport in terahertz quantum-cascade lasers," Phys. Rev. B **80**, 245316 (2009).
11. X. Huang, W. O. Charles, and C. Gmachl, "Temperature-insensitive long-wavelength ($\lambda \approx 14\mu$m) Quantum Cascade lasers with low threshold," Opt. Express **19**, 8297–8302 (2011).
12. X. Huang, Y. Chiu, W. O. Charles, and C. Gmachl, "Ridge-width dependence of the threshold of long wavelength ($\lambda \approx 14\mu$m) Quantum Cascade lasers with sloped and vertical side walls," Opt. Express **20**, 2539–2547 (2012).

#204573 - $15.00 USD Received 10 Jan 2014; revised 19 Feb 2014; accepted 27 Feb 2014; published 7 Mar 2014
(C) 2014 OSA

13. A. Gordon, C. Y. Wang, L. Diehl, F. X. Kärtner, A. Belyanin, D. Bour, S. Corzine, G. Höfler, H. C. Liu, H. Schneider, T. Maier, M. Troccoli, J. Faist, and F. Capasso, "Multimode regimes in quantum cascade lasers: From coherent instabilities to spatial hole burning," Phys. Rev. A **77**, 053804 (2008).

1. Introduction

As one of the most versatile and powerful mid-infrared laser sources, the quantum cascade (QC) laser has stimulated numerous research topics on their microscopic, waveguide and ridge site characteristics. For example, thermal effects were studied for GaInAs/AlInAs QC lasers, including a comparison of positive and negative polarity QC lasers with the same QC strctures [1], and thermal modeling with the in-plane and cross-plane thermal conductivities evaluated via microprobe photoluminescence [2]. Another example is the study on multi-transverse-mode operation and lateral spatial hole burning in QC lasers, including beam steering [3,4], coherent coupling and self-synchronization of multiple transverse modes [5, 6]. In thermal modeling, spatial hole burning modeling, multi-transverse-mode modeling, and general modeling for QC lasers, the current density is usually taken as laterally uniform [1,4,7], which is widely accepted in the QC laser field.

In QC lasers, resonant tunneling and longitudinal optical (LO) phonon scattering are regarded as the main scattering mechanisms contributing to electron transport, with the upper laser level typically featured by a LO-phonon scattering lifetime of $\sim$ ps. Moreover, stimulated optical emission depletes the upper laser level at a rate comparable to or even faster than the LO-phonon scattering rate in an efficient QC laser. It has been observed that stimulated optical emission also contributes to electron transport, leading to reduced resistance in QC lasers operating above laser threshold [8–10]. However, the microscopic features of the stimulated-optical-emission-assisted electron transport, with its effects on laser electrical and optical behaviors, have not been investigated yet. Here we show that in different transverse regions of the QC laser, the equivalent depletion lifetime by stimulated optical emission is in the order of ps and sub-ps, depending on the local photon density. Therefore, non-uniform photon density, corresponding to the transverse mode profile in a waveguide, leads to different local transport rates of electrons, and thus non-uniform current distribution. At the same time, the local current density determines the local optical gain and affects the local photon density in return. In this paper the self-consistent interaction process between the local electrons and local photons is investigated via two-dimensional (2D) modeling. The non-uniform current distribution in a QC laser due to stimulated optical emission is shown. Moreover, the corresponding spatial hole burning and the multi-transverse-mode operation process are also simulated based on this self-consistent electron-photon interaction picture.

2. Self-consistent 2D modeling of electron-photon interaction

Shown in Fig. 1 is the fundamental mode profile (calculated by the commercial software COMSOL) of a dry-etched QC laser emitting at $\sim 14\,\mu m$, with the QC structure reported earlier [11, 12] . The cross section of the active core is equally divided into $L \times M$ (here L = 9, M = 15) regions, by L partitions along the vertical out-of-plane direction and M partitions along the lateral in-plane direction, respectively. The current densities in these $L \times M$ regions are investigated via self-consistent 2D modeling based on microscopic rate equations, which takes into account the local interaction between electrons and photons.

The local sheet electron density $N_{3,l,m}(l = 1,2,\cdots,L,\ m = 1,2,\cdots,M)$ of the upper state (level 3) , sheet electron density $N_{2,l,m}$ of the lower state (level 2), and the local photon flux density $\varphi_{l,m}$ are calculated from a full set of rate equations for all the $L \times M$ individual regions of the active core,

#204573 - $15.00 USD Received 10 Jan 2014; revised 19 Feb 2014; accepted 27 Feb 2014; published 7 Mar 2014
(C) 2014 OSA

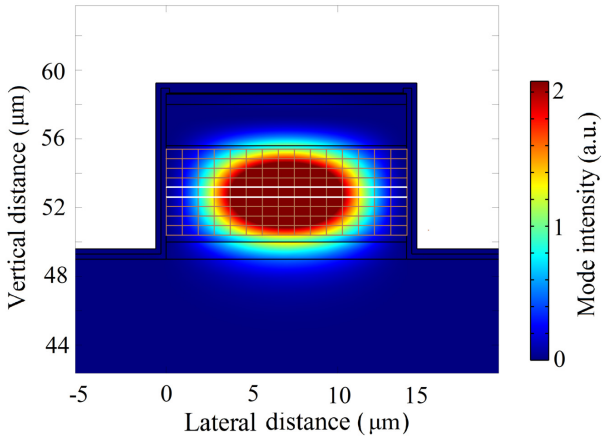

Fig. 1. 2D mode simulation for the fundamental transverse mode of a dry-etched QC laser emitting at $\sim 14\ \mu m$, with a ridge width of $14\ \mu m$. The active core is equally divided into 135 (9×15) regions. The two white lines are used to denote the center region along the vertical direction, which is studied in more detail.

$$\frac{dN_{3,l,m}}{dt} = \frac{J_{l,m}}{e} - \frac{N_{3,l,m}}{\tau_3} - \sigma_{32}\varphi p_{l,m}(N_{3,l,m} - N_{2,l,m}), \tag{1a}$$

$$\frac{dN_{2,l,m}}{dt} = \frac{N_{3,l,m}}{\tau_{32}} + \sigma_{32}\varphi p_{l,m}(N_{3,l,m} - N_{2,l,m}) - \frac{N_{2,l,m}}{\tau_2}, \tag{1b}$$

$$\frac{d\varphi}{dt} = \frac{c}{n}\varphi\{\frac{\Gamma\sigma_{32}\sum_{l=1}^{L}\sum_{m=1}^{M}[p_{l,m}(N_{3,l,m} - N_{2,l,m})]}{L_p\sum_{l,m}p_{l,m}} - \alpha\}, \tag{1c}$$

where $J_{l,m}$ is the local current density. φ is the photon flux density in the center element (with $l = \frac{L+1}{2}$, $m = \frac{M+1}{2}$). $p_{l,m}$ is the photon flux density of element (l,m) normalized by φ, i.e., $\varphi_{l,m} = p_{l,m}\varphi$. $p_{l,m}$ is calculated from the 2D mode simulation as shown in Fig. 1. $\tau_3 = 1.65ps$ and $\tau_2 = 0.23ps$ are LO phonon scattering lifetimes for the upper and lower laser levels, respectively. $1/\tau_{32} = 0.32ps^{-1}$ is the LO phonon scattering rate from the upper laser level to the lower laser level. $L_p = 67.3nm$ is the thickness of one stage of the active region and the injector. $\sigma_{32} = 2.66 \times 10^{-18}m^2$ is the cross section of optical transition. $\alpha = 31.7cm^{-1}$ is the optical loss, including waveguide loss and mirror loss. $\Gamma = 0.8$ is the mode confinement factor. In this model it is assumed that the current injection efficiency for the upper laser level is 1, changes in cross section σ_{32}, lifetimes τ_3, τ_2, and τ_{32} with the applied current/voltage are negligible, and τ_2 is smaller than τ_{32} for population inversion.

Here the lateral carrier diffusion term is not included, since the long wavelength ($\sim 14\ \mu m$) of the QC laser under investigation leads to a long diffusion lifetime $\sim 7\ ps$, estimated from [13]. Compared with the sub-ps depletion lifetime by stimulated optical emission (discussed in Section 3), the lateral diffusion effect is minor, and thus ignored for simplification.

Based on Eq. (1), with an injected current I, the calculation of the lateral current distribution is carried out by the self-consistent, iterative numerical approach as follows. In the k_{th} iteration

#204573 - $15.00 USD Received 10 Jan 2014; revised 19 Feb 2014; accepted 27 Feb 2014; published 7 Mar 2014
(C) 2014 OSA

step,

$$N_{3,l,m,k} = [\frac{J_{l,m,k}}{e} - \frac{N_{3,l,m,k-1}}{\tau_3} - \sigma_{32}\varphi_{k-1}p_{l,m}(N_{3,l,m,k-1} - N_{2,l,m,k-1})]\Delta t + N_{3,l,m,k-1}, \quad (2a)$$

$$N_{2,l,m,k} = [\frac{N_{3,l,m,k-1}}{\tau_{32}} + \sigma_{32}\varphi_{k-1}p_{l,m}(N_{3,l,m,k-1} - N_{2,l,m,k-1}) - \frac{N_{2,l,m,k-1}}{\tau_2}]\Delta t + N_{2,l,m,k-1}, \quad (2b)$$

$$\varphi_k = \{\frac{c}{n}\varphi_{k-1}[\frac{\Gamma\sigma_{32}\sum_{l=1}^{L}\sum_{m=1}^{M}[p_{l,m}(N_{3,l,m,k} - N_{2,l,m,k})]}{L_p\sum_{l,m}p_{l,m}} - \alpha]\}\Delta t + \varphi_{k-1}, \quad (2c)$$

with Δt the discretization step. Then the total effective lifetime $\tau_{3,l,m,k}^{\text{eff}}$ of the upper laser level, which includes the LO phonon scattering lifetime τ_3 and the depletion lifetime $\tau_{3,l,m,k}^{\text{ST}}$ by stimulated optical emission, is calculated by

$$\frac{1}{\tau_{3,l,m,k}^{\text{eff}}} = \frac{1}{\tau_3} + \frac{1}{\tau_{3,l,m,k}^{\text{ST}}}. \quad (3)$$

The following is the explicit expression of $\tau_{3,l,m,k}^{\text{eff}}$,

$$\tau_{3,l,m,k}^{\text{eff}} = \frac{N_{3,l,m,k}}{\frac{N_{3,l,m,k}}{\tau_3} + \sigma_{32}\varphi_k p_{l,m}(N_{3,l,m,k} - N_{2,l,m,k})}. \quad (4)$$

Then the calculation moves on to the $(k+1)_{th}$ iteration step. Since the local current density is determined by the sheet electron density of the upper laser state $N_{3,l,m,k}$ and its total effective lifetime $\tau_{3,l,m,k}^{\text{eff}}$, for all the elements in the same row (with the same l and different m) shown in Fig. 1, the injected current I is distributed among them according to $N_{3,l,m,k}/\tau_{3,l,m,k}^{\text{eff}}$. So the local current density $J_{l,m,k+1}$ for the $(k+1)_{th}$ step is estimated according to the results from the k_{th} step by

$$J_{l,m,k+1} = \frac{N_{3,l,m,k}/\tau_{3,l,m,k}^{\text{eff}}}{\sum_{m=1}^{M} N_{3,l,m,k}/\tau_{3,l,m,k}^{\text{eff}}} I/A, \quad (5)$$

where A is in-plane area of each element ($A =$ (cavity length)$\times$(ridge width)/ M) of the active core divided as shown in Fig. 1. With $J_{l,m,k+1}$ calculated from Eq. (5), $N_{3,l,m,k+1}$ and $\tau_{3,l,m,k+1}^{\text{eff}}$ are calculated via Eqs. (2) and (4) as in the k_{th} step, and the results will be used for $J_{l,m,k+2}$ calculation in the $(k+2)_{th}$ step following Eq. (5) again. The iteration is terminated when the calculation converges to the steady state for the photon flux density φ and the electron densities $N_{3,l,m}$ and $N_{2,l,m}$.

3. Non-uniform lateral current distribution

The calculated local current density is shown in Fig. 2 with the applied current 3 times the threshold current. The current density changes much more significantly in the lateral direction rather than in the vertical direction. So in the following, we focus on the lateral direction, by investigating regions with $l = (L+1)/2$, depicted between the two white lines in Fig. 1. The subscription "l" in parameters will be omitted for simplification.

In Fig. 3(a), the total effective depletion rate $1/\tau_{3,m}^{\text{eff}}$ of the upper laser level in different regions between the two white lines in Fig. 1 is shown at different applied current. Below laser threshold, with negligible photon flux density in the cavity, electron transport in all regions behaves in the same way with the upper laser level depleted by LO phonon scattering. Therefore, the same depletion rate is obtained in different regions as shown in Fig. 3(a). Equivalently, all these regions have the same resistance, and the input current is distributed uniformly among them, as shown in Fig. 3(b). When the laser reaches its threshold, in addition to depletion by LO photon scattering, the upper laser level is also depleted by stimulated optical emission with

#204573 - $15.00 USD Received 10 Jan 2014; revised 19 Feb 2014; accepted 27 Feb 2014; published 7 Mar 2014
(C) 2014 OSA

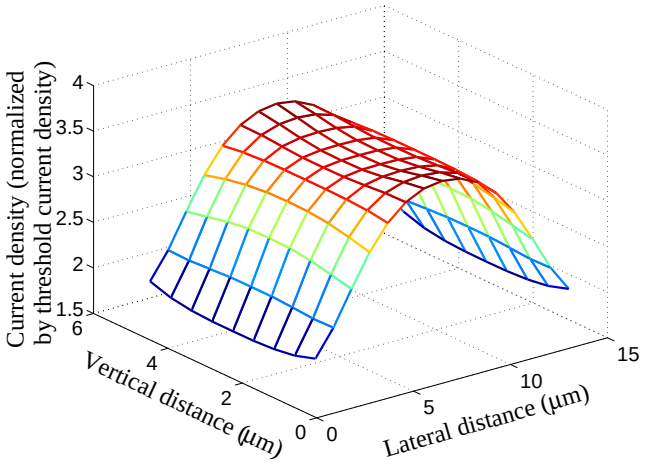

Fig. 2. Current density map of the cross section of the active core, with the QC laser at 3 times threshold.

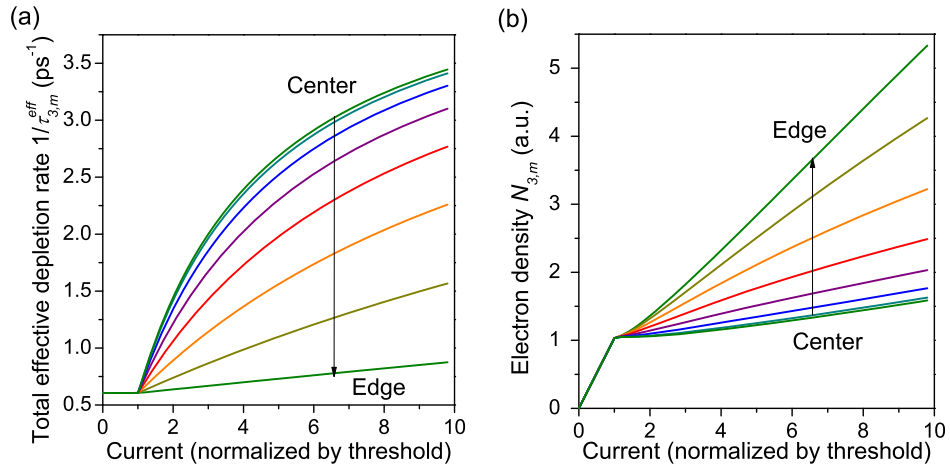

Fig. 3. (a) The total effective depletion rate, including LO phonon scattering and depletion by stimulated optical emission, of the upper laser level in different regions between the two white lines in Fig. 1. (b) Electron density of the upper laser level versus applied current in different regions.

non-negligible photon density, with the depletion rate depending on the local photon density (see Eq. (4)). As a result, in the center region of the mode, where the photon flux density is highest, the upper laser level has the fastest depletion rate, while in the edge region it has the slowest depletion rate due to a low local photon flux density (see Fig. 3(a)). Therefore, the electron density of the upper laser level in the center region is lowest due to fast depletion by stimulated optical emission, while that in the edge region is highest, as shown in Fig. 3(b). For example, when the applied current is 3 times the threshold for the QC structure under investigation, the total effective depletion rate of the upper laser level in the center region is 2.0 ps^{-1}

#204573 - $15.00 USD Received 10 Jan 2014; revised 19 Feb 2014; accepted 27 Feb 2014; published 7 Mar 2014
(C) 2014 OSA

while that in the edge is 0.67 ps^{-1}, and the electron density of the former is 60% that of the latter. Due to gain saturation under high photon flux density, the effective depletion rate in and close to the center region shows non-linear behavior at high applied current.

Shown in Fig. 4 is the lateral current distribution at different applied current at and above the threshold. The local current density of region m is determined by $N_{3,m}/\tau_{3,m}^{\text{eff}}$. The current density in the mode center is higher than that in the edge regions as the applied current exceeds the threshold current. For example, at 3 times threshold, the current density in the mode center region is 1.8 times the current density in the edge region. However, when the applied current is far above the threshold (>5 times the threshold here), the highest current density does not appear in the mode center due to its low local electron density, and the current distribution shows a camel back shape. Please note that in this work the upper end of the investigated current is as high as $\sim$10 times the threshold with a corresponding photon flux density of $\sim 3\times 10^{27} s^{-1}\cdot cm^{-2}$, in order to provide a full picture of current distribution characteristics over a wide operation range, though in an actual device the operation current range is normally much narrower.

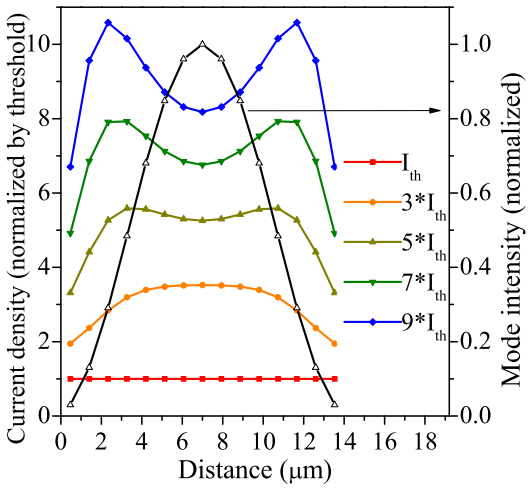

Fig. 4. Lateral current distribution with different injected current ranging from threshold current to 9 times threshold current. Also displayed is the lateral mode profile.

4. Spatial hole burning model

With the non-uniform current density due to stimulated optical emission discussed in Section 3, the corresponding gain distribution in the active core is calculated and shown in Fig. 5, again with an applied current 3 times the threshold current as an example. The minimum of the gain appears in the mode center due to spatial hole burning, and the gain changes much more significantly in the lateral direction rather than in the vertical direction, similar to the change trend of current density shown in Fig. 2. Again, we focus on the lateral direction by investigating the regions depicted between the two white lines in Fig. 1, and the lateral hole burning at different applied current at and above the threshold is shown in Fig. 6(a). As expected, along with the increasing current and photon density, the gain in the mode center is depleted by strong stimulated optical emission, while the gain in the edge region is significantly higher.

The spatial hole burning simulated with non-uniform current density due to stimulated optical emission is compared with the simulation based on uniform current distribution in Fig. 6(b), both at 3 times threshold as an example. On account of the non-uniformity of the lateral

#204573 - $15.00 USD Received 10 Jan 2014; revised 19 Feb 2014; accepted 27 Feb 2014; published 7 Mar 2014
(C) 2014 OSA

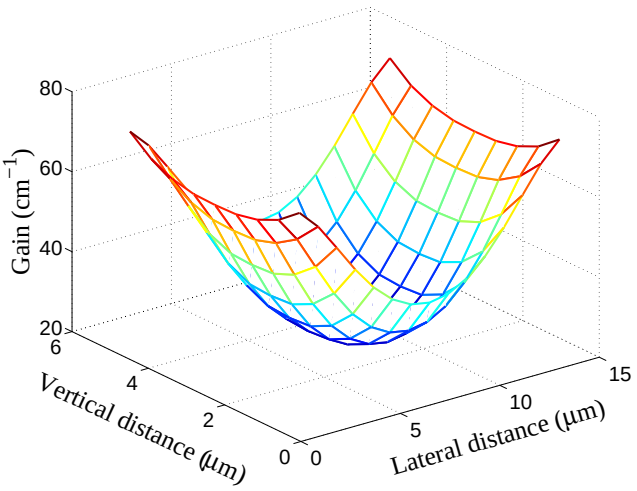

Fig. 5. Gain map of the cross section of the active core, with the QC laser at 3 times threshold.

current density, the local gain is increased by 6.7% in the mode center region and decreased by 35.6% in the edge region, compared with modeling results with the assumption of uniform current density. This big difference means non-negligible effects of lateral current non-uniformity for simulations and analysis of spatial gain hole burning. Moreover, in the following it will be shown that the simulation of multi-transverse-mode operation is largely improved with the non-uniform current density model.

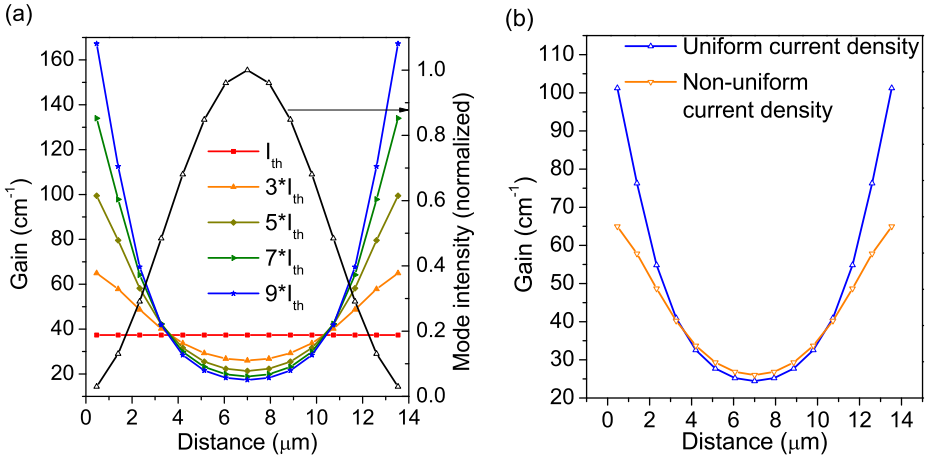

Fig. 6. (a) Lateral hole burning simulation results. (a) Lateral hole burning with different injected current. Also displayed is the lateral mode profile. (b) Comparison of lateral spatial hole burning modeling, with uniform current density assumption and non-uniform current density due to stimulated optical emission, respectively.

#204573 - $15.00 USD Received 10 Jan 2014; revised 19 Feb 2014; accepted 27 Feb 2014; published 7 Mar 2014
(C) 2014 OSA

5. Multi-transverse-mode operation

Multi-transverse-mode operation in QC lasers leads to interesting phenomena including beam steering due to competition between multiple transverse modes [3, 4], and coherent coupling and self-synchronization of multiple transverse modes due to phase locking [5, 6].

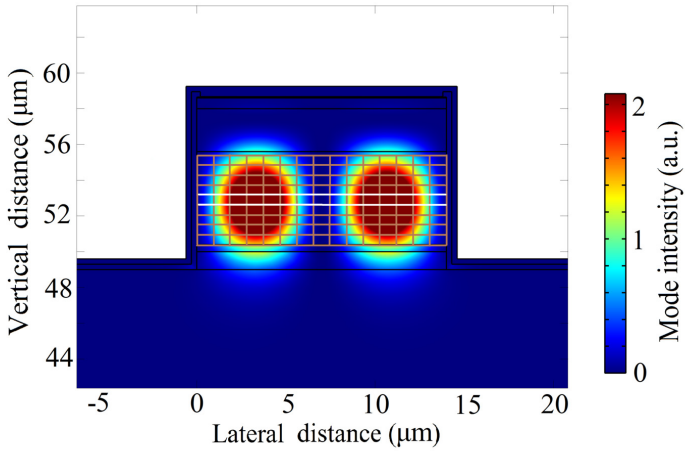

Fig. 7. 2D simulation results of the first higher-order mode in the same QC structure as depicted in Fig. 1. The active core is also equally divided into 135 (9×15) regions. The two white lines denoted the center region in the vertical direction.

Based on the self-consistent electron-photon interaction picture here, multiple mode operation is simulated with non-uniform current distribution. Here we study the simplest scenario, with the fundamental mode (see Fig. 1) and the first higher-order mode (see Fig. 7) coexisting and competing for the gain. First, Eq. (1) is modified to include the first higher-order mode,

$$\frac{dN_{3,l,m}}{dt} = \frac{J_{l,m}}{e} - \frac{N_{3,l,m}}{\tau_3} - \sigma_{32}(\varphi p_{l,m} + \varphi' p'_{l,m})(N_{3,l,m} - N_{2,l,m}), \tag{6a}$$

$$\frac{dN_{2,l,m}}{dt} = \frac{N_{3,l,m}}{\tau_{32}} + \sigma_{32}(\varphi p_{l,m} + \varphi' p'_{l,m})(N_{3,l,m} - N_{2,l,m}) - \frac{N_{2,l,m}}{\tau_2}, \tag{6b}$$

$$\frac{d\varphi}{dt} = \frac{c}{n}\varphi\{\frac{\Gamma\sigma_{32}\sum_{l=1}^{L}\sum_{m=1}^{M}[p_{l,m}(N_{3,l,m}-N_{2,l,m})]}{L_p\sum_{l,m}p_{l,m}} - \alpha\}, \tag{6c}$$

$$\frac{d\varphi'}{dt} = \frac{c}{n}\varphi'\{\frac{\Gamma'\sigma_{32}\sum_{l=1}^{L}\sum_{m=1}^{M}[p'_{l,m}(N_{3,l,m}-N_{2,l,m})]}{L_p\sum_{l,m}p'_{l,m}} - \alpha'\} \tag{6d}$$

where φ' is the peak photon flux density of the first higher-order mode, with $p'_{l,m}$ the photon flux density of element (l,m) normalized by φ', i.e., $\varphi'_{l,m} = p'_{l,m}\varphi'$. $p'_{l,m}$ is calculated from the 2D optical mode simulation as shown in Fig. 7. Γ' and α' are the mode confinement factor and the optical loss for the first higher-order mode, respectively. The other parameters related to the fundamental mode were explained earlier with Eq. (1). Based on Eq. (6), the same temporal discretization and iterative approach is used as in Section 2 for the single-transverse-mode

#204573 - $15.00 USD Received 10 Jan 2014; revised 19 Feb 2014; accepted 27 Feb 2014; published 7 Mar 2014
(C) 2014 OSA

scenario, and discretized equations are obtained as,

$$N_{3,l,m,k} = [\frac{J_{l,m,k}}{e} - \frac{N_{3,l,m,k-1}}{\tau_3} - \sigma_{32}(\varphi_{k-1}p_{l,m} + \varphi'_{k-1}p'_{l,m})(N_{3,l,m,k-1} - N_{2,l,m,k-1})]\Delta t + N_{3,l,m,k-1}, \tag{7a}$$

$$N_{2,l,m,k} = [\frac{N_{3,l,m,k-1}}{\tau_{32}} + \sigma_{32}(\varphi_{k-1}p_{l,m} + \varphi'_{k-1}p'_{l,m})(N_{3,l,m,k-1} - N_{2,l,m,k-1}) - \frac{N_{2,l,m,k-1}}{\tau_2}]\Delta t + N_{2,l,m,k-1}, \tag{7b}$$

$$\varphi_k = \{\frac{c}{n}\varphi_{k-1}[\frac{\Gamma\sigma_{32}\sum_{l=1}^{L}\sum_{m=1}^{M}[p_{l,m}(N_{3,l,m,k} - N_{2,l,m,k})]}{L_p\sum_{l,m}p_{l,m}} - \alpha]\}\Delta t + \varphi_{k-1}, \tag{7c}$$

$$\varphi'_k = \{\frac{c}{n}\varphi'_{k-1}[\frac{\Gamma\sigma_{32}\sum_{l=1}^{L}\sum_{m=1}^{M}[p'_{l,m}(N_{3,l,m,k} - N_{2,l,m,k})]}{L_p\sum_{l,m}p'_{l,m}} - \alpha']\}\Delta t + \varphi'_{k-1}. \tag{7d}$$

Here the corresponding total effective lifetime $\tau^{\text{eff}}_{3,l,m,k}$ of the upper laser level (in the k_{th} iteration step), which includes the LO phonon scattering lifetime τ_3 and the depletion lifetime $\tau^{\text{ST}}_{3,l,m,k}$ by stimulated optical emission from the fundamental mode and the first higher mode, is calculated similar to Eq. (4),

$$\tau^{\text{eff}}_{3,l,m,k} = \frac{N_{3,l,m,k}}{\frac{N_{3,l,m,k}}{\tau_3} + \sigma_{32}(\varphi_k p_{l,m} + \varphi'_k p'_{l,m})(N_{3,l,m,k} - N_{2,l,m,k})}. \tag{8}$$

Then the calculation moves on to the $(k+1)_{\text{th}}$ step. Again the local current density for the $(k+1)_{\text{th}}$ step is determined by the electron density of the upper laser state $N_{3,l,m,k}$ and its total effective lifetime $\tau^{\text{eff}}_{3,l,m,k}$ through Eq. (5).

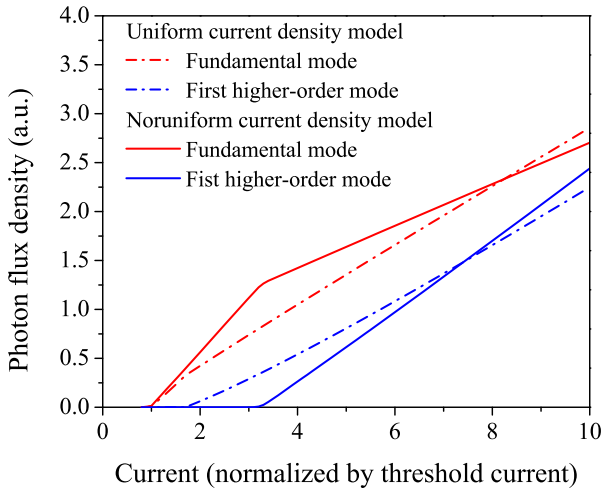

Fig. 8. QC laser operation with the fundamental mode and the first higher-order mode. Simulations were conducted in two ways. One is based on the assumption that the current distribution in the active core is uniform, and the other is based on the self-consistent process of electron-photon interaction which leads to non-uniform current density.

Photon generation from the fundamental mode and the first higher-order mode is simulated in Fig. 8. Moreover, simulation results based on the non-uniform current density due to stimulated optical emission, the focus of this work, are compared with the results from the uniform current

#204573 - $15.00 USD Received 10 Jan 2014; revised 19 Feb 2014; accepted 27 Feb 2014; published 7 Mar 2014
(C) 2014 OSA

density model. With the uniform current density model, the first higher-order mode starts to lase at 1.8 times the threshold of the fundamental mode. But as shown earlier (see Fig. 6(b)), spatial hole burning with fundamental mode only is overestimated from the uniform current density model. In fact, the gain available to the first higher-order mode is lower when taking into account the non-uniform distribution of lateral current density. Specifically, the first higher-order mode starts to lase at 3.3 times the threshold of the fundamental mode, which is much higher than 1.8 times the threshold predicted by the uniform current density model.

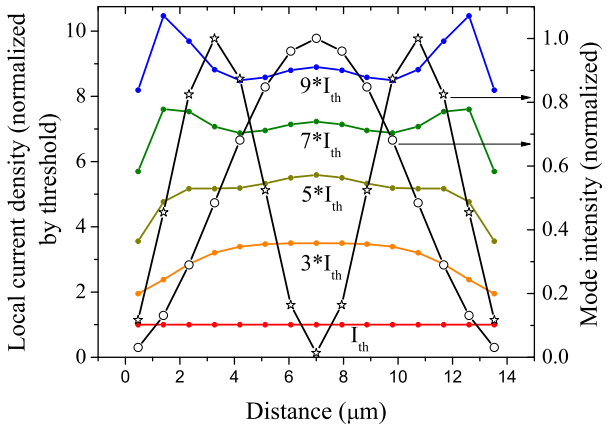

Fig. 9. Local current densities with different injected current ranging from threshold current to 9 times threshold current. Also displayed are the lateral mode profiles of the fundamental mode and the first higher-order mode. The first higher-order mode starts to lase at 3.3 times the threshold of the fundamental mode.

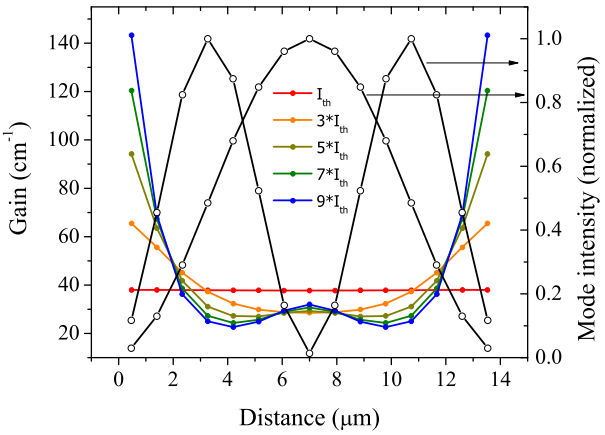

Fig. 10. Spatial hole burning with different injected current. Also displayed are the lateral mode profiles of the fundamental mode and the first higher-order mode.

The local current density is shown in Fig. 9, with different injected current ranging from threshold current to 9 times threshold current, for regions between the two white lines in Figs. 1 and 7. With the applied current below 3.3 times the threshold, only the fundamental mode exists, and the current density curves are the same as those shown in Fig. 4. The first higher-order mode starts to lase at 3.3 times the threshold (of the fundamental mode). With both transverse modes

#204573 - $15.00 USD Received 10 Jan 2014; revised 19 Feb 2014; accepted 27 Feb 2014; published 7 Mar 2014
(C) 2014 OSA

lasing, the uniformity of current density shown in Fig. 9 is improved compared with single mode operation (see Fig. 4), since here two modes make better use of the gain medium.

Shown in Fig. 10 is the lateral hole burning at different injected current. Compared with spatial hole burning with single mode operation shown in Fig. 6(a), here two dips are seen, corresponding to features of the combined fundamental and first higher-order modes.

Here the simulation is carried out for QC laser operation with the fundamental mode and first higher-order mode coexisting. Nevertheless, it can be extended to the situation of laser operation with more higher-order modes.

6. Conclusion

Based on a microscopic rate equation model for electron-photon interaction, the effectiveness of stimulated optical emission as a fast way for electron transport in QC lasers has been disclosed quantitatively, with a depletion lifetime of sub-ps. The non-uniform current distribution, resulting from stimulated optical emission, is studied based on this model. Significant non-uniformity was shown in the lateral direction from the simulation results, e.g., at 3 times the threshold for the QC structure under investigation, the current density in the mode center region is 1.8 times the current density in the edge region.

2D simulation of spatial hole burning is modified correspondingly, with non-uniform current distribution due to stimulated optical emission. Here with the applied current 3 times the threshold, the local gain is increased by 6.7% in the mode center region and decreased by 35.6% in the edge region, compared to a model with uniform current density.

Furthermore, multi-transverse-mode operation of a QC laser is investigated. It is shown that with the non-uniformity of current distribution taken into account, the lasing properties are significantly different from the model with uniform current density. For the QC structure used here, the first higher-order mode starts to lase at 3.3 times the threshold of the fundamental mode, which is much higher than 1.8 times the threshold predicted by the uniform current density model.

The model with non-uniform lateral current distribution provides a microscopic perspective on electrical and optical properties of QC lasers. With the microscopic information on local current density, it is expected to improve calculation of thermal effects in a QC laser. Moreover, based on the improved simulation of multi-mode operation, this model will also lead to a better understanding of interesting phenomena including beam steering [3, 4] and coherent coupling of multiple transverse modes [5, 6].

Acknowledgments

This work was supported in part by MIRTHE (NSF-ERC).

#204573 - $15.00 USD Received 10 Jan 2014; revised 19 Feb 2014; accepted 27 Feb 2014; published 7 Mar 2014
(C) 2014 OSA

128.112.33.188 {ts '2018-04-30 09:57:57'}